The shear fracture of dual-phase steel

Ji Hoon Kim [a], Ji Hyun Sung [b], Kun Piao [c], R.H. Wagoner [c,*]

[a] Materials Deformation Group, Korea Institute of Materials Science, 797 Changwondaero, Changwon, Gyeongnam 642-831, South Korea
[b] Green Transformation Technology Center, Daegu-Gyeongbuk Technology Application Division, Korea Institute of Industrial Technology, 711 Hosandong, Dalseogu, Daegu 704-230, South Korea
[c] Department of Materials Science and Engineering, The Ohio State University, 2041 College Road, Columbus, OH 43210, USA

ARTICLE INFO

ABSTRACT

Unexpected fractures at high-curvature die radii in sheet forming operations limit the adoption of advanced high strength steels (AHSS) that otherwise offer remarkable combinations of high strength and tensile ductility. Identified as "shear fractures" or "shear failures," these often show little sign of through-thickness localization and are not predicted by standard industrial simulations and forming limit diagrams. To understand the origins of shear failure and improve its prediction, a new displacement-controlled draw-bending test was developed, carried out, and simulated using a coupled thermo-mechanical finite element model. The model incorporates 3D solid elements and a novel constitutive law taking into account the effects of strain, strain rate, and temperature on flow stress. The simulation results were compared with companion draw-bend tests for three grades of dual-phase (DP) steel over a range of process conditions. Shear failures were accurately predicted without resorting to damage mechanics, but less satisfactorily for DP 980 steel. Deformation-induced heating has a dominant effect on the occurrence of shear failure in these alloys because of the large energy dissipated and the sensitivity of strain hardening to temperature increases of the order of 75 °C. Isothermal simulations greatly overestimated the formability and the critical bending ratio for shear failures, thus accounting for the dominant effect leading to the inability of current industrial methods to predict forming performance accurately. Use of shell elements (similar to industrial practice) contributes to the prediction error, and fracture (as opposed to strain localization) contributes for higher-strength alloys, particularly for transverse direction tests. The results illustrate the pitfall of using low-rate, isothermal, small-curvature forming limit measurements and simulations to predict the failure of high-rate, quasi-adiabatic, large-curvature industrial forming operations of AHSS.

© 2011 Elsevier Ltd. All rights reserved.

1. Introduction

From the start of mass production until approximately twenty years ago, establishing a sheet forming operation for a new part shape required multiple stages of experimental die tryout, often over a period of many months or years. This process changed radically with the advent of faster computers and nonlinear finite element methods, which allowed sufficiently accurate prediction of forming strains. These strains were then compared with forming limit diagrams to detect problem configurations and suggest die improvements, all before any dies were made. Today, virtually all automotive sheet-formed

---

* Corresponding author. Tel.: +1 614 292 2079; fax: +1 614 292 6530.
E-mail address: wagoner.2@osu.edu (R.H. Wagoner).

parts are made without resort to preliminary tools and with little or no die tryout, with the result that successful dies can be made in weeks.

The dramatic success of these methods was built on twin foundations of stress/strain analytical techniques and experimental techniques to construct forming limit diagrams. Less directly, these methods took advantage of little-changing classes of materials employed, mainly low-strength steels, high-strength/low alloy steels, and several aluminum alloys. Experience verified that nearly all splitting failures occurred in gently-curved regions by a process of plastic localization under various combinations of biaxial tensile stresses.

Recently, a new class of materials has been increasingly considered and/or adopted for automotive sheet forming. These "advanced high strength steels" (AHSS) (Wagoner, 2006), offer remarkable combinations of ultimate tensile strength and tensile ductility, thus enabling mass reduction, reduced fuel consumption, improved performance, and reduction of noxious emissions. The most common AHSS currently is dual-phase (DP) steel, with other grades including transformation-inducted plasticity (TRIP) steels, twinning-induced plasticity (TWIP) steels, and complex-phase (CP) steels.

When the usual simulation and experimental methods were employed to design dies for DP steel, they failed to predict dramatic failures that occurred in high-curvature (low bending ratio, R/t) regions (Stoughton et al., 2006; Xia et al., 2006; Heimbuch, 2006; Matlock, 2006; Bhattacharya, 2006). Dubbed "shear failure" or "shear fracture" (Chen et al., 2009; Sklad, 2008; Walp et al., 2006), the appearance of these failures differs in two respects from the typical ones observed in the past for traditional sheet forming materials:

(1) They occur where material is drawn over a sharp die radius, for example over a long, cylindrical feature.
(2) It is often difficult to see significant thinning near the fracture, as is characteristic of plastic localization in gently-curved regions.

The appearance of shear fractures, and particularly the inability to understand and predict them (Sriram and Urban, 2003; Wu et al., 2006), has inhibited the adoption of AHSS and delayed the conferring of the many promised societal advantages. Conventional wisdom attributed the new types of failure to a unique microstructurally-related fracture mechanism, such as unusual void growth near the large, hard particles in dual-phase (DP) steels (Matlock, 2006; Choi et al., 2009; Kim et al., 2009; Chen et al., 2010).

The authors recently reproduced shear failures for several grades of DP steels using a novel draw-bend fracture (DBF) test that controls the displacement of two actuators in order to assure one-directional motion of the sheet over the die radius, similar to the conditions in sheet forming operations that cause shear fracture (Wagoner et al., 2009a,b; Sung et al., in preparation). The test is based on a modification of a draw-bend configuration that has been used for friction (Wenzloff et al., 1992; Vallance and Matlock, 1992) and springback test (Wagoner et al., 1997; Li et al., 1999; Carden et al., 2002), and an earlier fracture measurement (Damborg et al., 1997, 1998). Three types of failures were identified visually, as illustrated
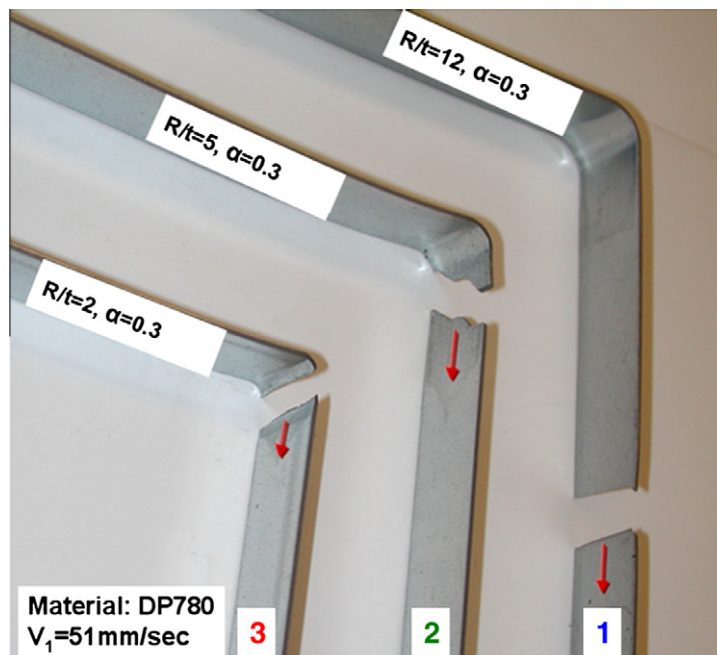

Fig. 1. The three DBF failures (reproduced from Sung et al., 2010b).

in Fig. 1, according to the location of the failure. Type 1 is a normal tensile localization failure caused by stretching without bending and unbending; it occurs in the front leg away from any material that was ever in contact with the roller. Type 3 is a shear failure; it occurs on the roller or at the tangent departure point near the center of the strip (not at the edge) and propagates nearly perpendicular to the longitudinal/pulling direction. Type 2 is a transitional failure that appears to start at the tangent departure point or slightly below it but which then propagates along a non-perpendicular path through material that has passed over the roller. Discerning Type 3 and 2 is not always easy when the failure location is close to the tangent departure point. For those cases, the direction of the propagation path is used to help identify the failure type in these cases. The DBF tests showed the expected shear failures for smaller bending ratios (R/t, where R is the tool radius and t is the initial sheet thickness). However, they also showed that higher strain rates for a set of constant R/t tests caused a transition to shear fracture. Local temperatures in the bending and unbending areas away from the final fracture surface were measured up to 100 °C at peak strain rates of the order of 1/s. For comparison, peak strain rates encountered in industrial forming operations are approximately 10/s (Fekete, 2009). A second surprising result was found: the reduction of area for most tested alloys (and all alloys tested in the RD direction) was similar for shear failures and tensile failures (Sung et al., in preparation). These observations led to the hypothesis that the unpredicted shear failures of AHSS observed in practice are principally related to deformation-induced heating that is unaccounted for with standard industrial methods, rather than a special fracture mechanism related to the microstructures of these alloys (Sung et al., 2010).

Standard forming analysis relies on isothermal finite element simulations using shell elements to predict the strains encountered (Hora and Tong, 2008). In view of the hypothesis stated above, such methods may have two shortcomings when applied to forming AHSS at standard industrial rates:

(1) The isothermal assumption becomes progressively less accurate as the material deformation energy increases, as is the case for materials with high strength and high ductility (Krauer and Hora, 2009). DP steels were recently shown to have temperature-dependent strain hardening in the temperature range of interest, which magnifies the effect.

(2) Shell elements exhibit inaccurate behavior for R/t ratios less than 5–6 (Li et al., 2002). That is usually not a serious problem for sheet forming analysis when failure occurs in gently-curved regions, but may become critical for the failure modes of AHSS in regions of small R/t.

Standard forming limit diagrams, FLD, (Keeler and Backofen, 1963; Wagoner et al., 1989) face similar deviations related to AHSS forming. Such diagrams describe experimental limiting strain states based on the onset localized deformation, or necking. The limiting strains are measured using a Nakajima dome test (Nakajima et al., 1971; Hecker, 1974; Ghosh, 1975), typically with a 50 mm radius, giving R/t ratios of 25–50 for typical sheet thicknesses of 1–2 mm, i.e., very gentle curvature. The tests are conducted at very low strain rate which maintains a thermal condition close to isothermal. While these conditions are consistent with those adopted for the simulations, they differ significantly from those encountered in industrial practice.

Significant recent effort has been applied to predict shear fractures by the use of the fracture mechanics (Bai and Wierzbicki, 2008; Chen et al., 2010; Li et al., 2010; Ma et al. 2010), instability theory (Hudgins et al., 2010), and micromechanical modeling (Kadkhodapour et al., 2011; Krempaszky et al., 2007), However, the effect of deformation heating has been neglected in these approaches. As will be shown later in this paper, deformation heating is the dominant physical cause promoting shear fracture.

In order to probe the hypothesis that shear failure is related to deformation-induced heating, a coupled thermo-mechanical finite element model using solid elements was constructed in the current work to simulate the draw-bend test. Comparisons of the thermo-mechanical model with corresponding isothermal ones reveal the magnitude of the deformation heating effect. Similar comparisons between simulations using shell and solid elements help to quantify those differences. The draw-bend fracture test is briefly introduced in the next section and the thermo-mechanical finite element model is presented in Section 3. Results, discussion, and conclusions are presented in Sections 4 and 5.

2. Draw-bend fracture test

In the recently-developed DBF test, Fig. 2 (Sung et al., in preparation), a sheet strip is bent 90° over a fixed roller with the both ends clamped in grips that are connected to actuators. The front grip moves at a constant speed, V_1, and the back grip moves at a constant speed, V_2, giving a fixed ratio of V_2/V_1. The difference $V_2 - V_1$ controls the stretching rate of the strip specimen. FE results show that the maximum strain rate in the test, $\dot{\varepsilon}_{max}$, can be approximated as follows (see Appendix A for derivation):

$$\dot{\varepsilon}_{max} = \frac{V_1(\text{mm/s})}{3t(\text{mm})} \ln(1 + t/R). \tag{1}$$

The control of V_1 and V_2 ensures that the movement of the sample over the die radius is consistently in the forward direction, thus fracture always occurs toward the front leg of the specimen. This is not guaranteed for previously-used back-force-controlled DBF tests (Damborg et al., 1997, 1998; Hudgins et al., 2010), leading to difficult-to-interpret results.

Sheet samples, 25.4 mm wide by 559 mm long were used with the strip axis parallel to the sheet rolling direction. Tests were performed with fixed (not turning) rollers having diameters between 6.3 and 38.1 mm, and lubricated with a standard
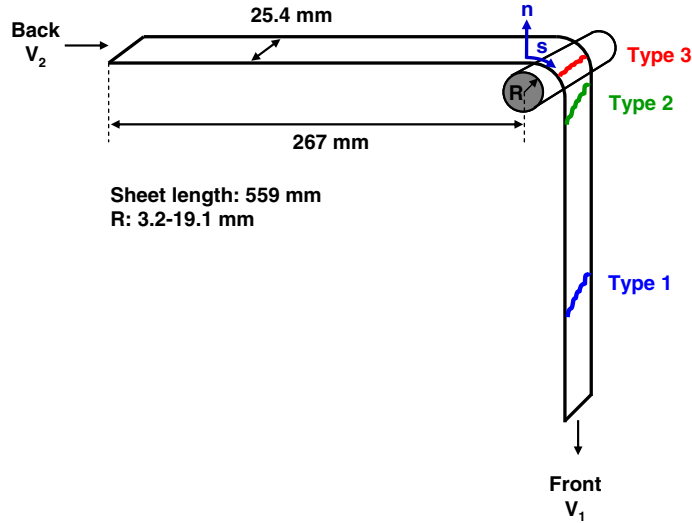
Fig. 2. Schematic of the draw-bend fracture test and types of failures observed.

stamping lubricant to mimic interfacial conditions in typical forming processes. Grip displacements (U_1 and U_2 for front, pulling grip and back, dragged grip, respectively) were controlled and the loads (F_1 and F_2 for front and back forces, respectively) at the grips were measured. The tests proceeded until sample failure, either by tensile plastic localization/necking near the tangent point where the strip leaves contact with the roller or by shear failure in the straight strip area on the forward, pulling side, depending on the material properties and testing conditions. More details of the DBF test, the experimental procedures, and results for the alloys used here can be found elsewhere (Sung et al., 2010a, in preparation).

3. Constitutive behavior

Three AHSSs were tested and simulated: DP590, DP780, and DP980 (the numbers refer to nominal ultimate tensile strengths), Table 1. The chemical compositions have been presented elsewhere (Sung et al., 2010a, in preparation).

A new empirical work hardening constitutive model, "H/V model" (Sung et al., 2010a) was constructed from three multiplicative functions relating to temperature-dependent strain hardening, strain-rate sensitivity, and temperature softening, as follows:

$$\sigma = \sigma(\varepsilon, \dot{\varepsilon}, T) = f(\varepsilon, T) \cdot g(\dot{\varepsilon}) \cdot h(T), \tag{2}$$

where σ is the tensile flow stress, ε is the plastic strain, $\dot{\varepsilon}$ is the strain rate, and T is the temperature. The functions, f, g, and h, representing strain hardening, strain-rate sensitivity, and temperature softening, respectively, are given by

$$f(\varepsilon, T) = \alpha(T)H_{HV}\varepsilon^{n_{HV}} + (1 - \alpha(T)) \cdot V_{HV}\left(1 - A_{HV}e^{-B_{HV}\varepsilon}\right), \tag{3}$$

$$g(\dot{\varepsilon}) = \left(\frac{\dot{\varepsilon}}{\dot{\varepsilon}_0}\right)^{a\log\dot{\varepsilon}+b}, \tag{4}$$

$$h(T) = 1 - \beta(T - T_R), \tag{5}$$

where $\alpha(T) = \alpha_1 - \alpha_2(T - T_R)$, T_R is a reference temperature, $\dot{\varepsilon}_0$ is a reference strain rate, and A_{HV}, B_{HV}, H_{HV}, V_{HV}, a, b, n_{HV}, α_1, α_2, and β are material constants. The best-fit constants for the three materials in Table 2 were obtained as described in Sung

Table 1
Standard tensile properties of the three DP steels tested in the rolling direction.

Material	DP590	DP780	DP980
Thickness (mm)	1.40	1.40	1.43
Yield stress (MPa, 0.2% offset)	369	472	552
Ultimate tensile strength (MPa)	624	796	972
Uniform elongation (%)	15.4	13.0	9.9
Fracture strain (%)	24.7	17.6	13.9
n-Value	0.20	0.18	0.13
r-Value	0.84	0.97	0.76

Table 2
H/V model material constants for the three DP steels.

Material	f_H	f_V	Temp. constant	Rate
DP590	H_{HV}: 1051 MPa n_{HV}: 0.179	V_{HV}: 643.9 MPa A_{HV}: 0.576 B_{HV}: 22.44	α_1: 0.818 α_2: 0.002 β: 2.7×10^{-4}	a: 2.0×10^{-3} b: 1.0×10^{-2} $\dot{\varepsilon}_0$: 0.001/s
DP780	H_{HV}: 1655 MPa n_{HV}: 0.213	V_{HV}: 752.1 MPa A_{HV}: 0.265 B_{HV}: 30.31	α_1: 0.507 α_2: 0.002 β: 5.8×10^{-4}	a: 3.0×10^{-3} b: 1.2×10^{-2} $\dot{\varepsilon}_0$: 0.001/s
DP980	H_{HV}: 1722 MPa n_{HV}: 0.154	V_{HV}: 908.1 MPa A_{HV}: 0.376 B_{HV}: 39.64	α_1: 0.586 α_2: 0.001 β: $.9 \times 10^{-4}$	a: 2.1×10^{-3} b: 8.6×10^{-3} $\dot{\varepsilon}_0$: 0.001/s
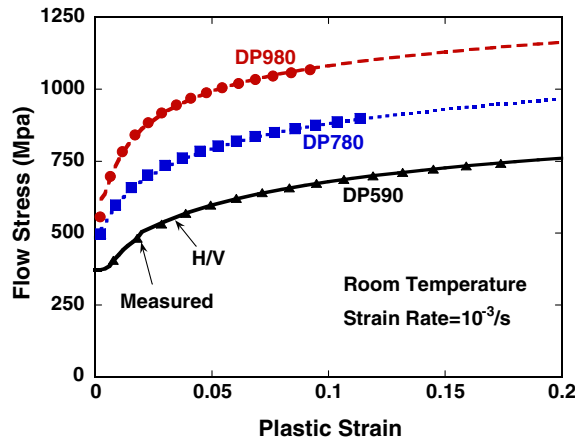
Fig. 3. Room temperature stress–strain response of three DP steels deformed isothermally in tension at 10^{-3}/s, experiments vs. H/V model fit to various temperatures and strain rates.

Table 3
The best-fit coefficients of the modified H/V model.

Material	f_H	f_V	Temp. constant	R^2
DP590	H_{HV}: 1329 MPa n_{HV}: 0.260	V_{HV}: 721.2 MPa A_{HV}: 0.407 B_{HV}: 14.83	α_1: 0.377 α_2: 0.005 β: 9.6×10^{-5}	0.996
DP780	H_{HV}: 1544 MPa n_{HV}: 0.257	V_{HV}: 946.7 MPa A_{HV}: 0.312 B_{HV}: 19.84	α_1: 0.401 α_2: 0.005 β: 0.0015	0.997
DP980	H_{HV}: 1676 MPa n_{HV}: 0.190	V_{HV}: 1118 MPa A_{HV}: 0.317 B_{HV}: 26.60	α_1: 0.437 α_2: 05 β: 01	0.998

et al. (2010a). The tests conducted by Sung et al. include the tensile tests at 25, 50, and 100 °C at a strain rate of 10^{-3}/s to reveal strain hardening as a function of temperature, along with strain rate jump tests to reveal the strain-rate sensitivity. The flow stress curves at room temperature and a strain rate of 10^{-3}/s reproduced using (2) are shown in Fig. 3 along with the experimental data. As shown in Fig. 3, the constitutive model does not fit the low-strain data as well as for the remaining strain range. For simulation purpose, the actual experimental data were used for plastic strains less than 0.02.

The von Mises yield surface and the isotropic hardening rule were assumed for simplicity and in view of plastic anisotropy parameters not greatly different from unity and RD and TD tensile tests having nearly identical hardening law (Sung et al., in preparation).

Extrapolations from the tensile-fit H/V model to large strain has been verified at room temperature by balanced biaxial tests, but no such verification has been possible at higher temperatures. In order to allow for the possibility that more significant softening occurs at high strains and high temperatures (via more Voce-like behavior), a "Modified H/V Model" was constructed. For each material, the same experimental data ($\varepsilon = .02 - 0.2$, $\dot{\varepsilon} = 0.001$) at 25, 50 and 100 °C was combined

with three fictitious stress–strain points at strains of 0.9, 0.95, and 1.0 for which the stresses were computed as follows. At 100 °C, the stresses were taken from the Voce part of the normal H/V fit, i.e. the stresses were computed as if alpha were zero in Eq. (3). At 50 °C, the stresses for the fictitious points were computed as if alpha were 1/2 in Eq. (3). At 25 °C, the fictitious stress values were taken from the normal H/V fit at these high strains. The new data set, including the fictitious points, was then re-fit to obtain new H/V parameters as shown in Table 3. In the table, the coefficient of determination, *R*-squared, is defined as:

$$R^2 = 1 - \frac{\sum_i (\sigma_i - \sigma_{i,\text{HV}})^2}{\sum_i (\sigma_i - \bar{\sigma})^2},$$ (6)

where σ_i is the measured stress, $\bar{\sigma}$ is the average, and $\sigma_{i,\text{HV}}$ is the H/V model prediction. The overall effect of these changes is to accelerate the transition from Hollomon hardening at low temperatures to Voce temperatures at 100 °C, while maintaining good agreement with all of the tensile data.

4. Thermo-mechanical finite element model

A thermo-mechanical finite element model of the draw-bend test was developed using Abaqus 6.7 Standard, as shown in Fig. 4. To account for the out-of-plane stress and deformation heating from bending and stretching at small radii, thermo-mechanical 3D solid elements (C3D8RT) were employed with five element layers through the thickness. Elements of size of 0.5 mm in the longitudinal direction, 1.8 mm in the width direction, 0.28 mm in the thickness direction were used in the region where bending and unbending take place. The model has 12846 elements, 22342 nodes, and 57916 degrees of freedom. The roller (which was fixed for all simulations) was modeled with rigid 3D solid elements with only temperature degrees of freedom. Half of the strip was modeled by applying symmetric boundary conditions along the longitudinal symmetry line shown in Fig. 4.

In order to allow tensile localization to occur naturally, the finite element mesh was perturbed slightly to remove the strict mathematical regularity shown in Fig. 4, and to make contact–non-contact transitions smoothes as nodes enter and leave contact over the cylindrical tool. First, the lateral rows of nodes that will contact the roller (across the width of the strip specimen) were inclined by 3° from the width direction to avoid full rows of nodes entering and leaving contact simultaneously. Second, the position of each node in the whole strip surface away from contact was perturbed in the in-plane direction by a maximum of 5% of the corresponding element dimensions, and in the thickness direction by a maximum of 1% of the sheet thickness. The statistical population of perturbations was made by random thickness choices in the allowed range in terms of r, θ (radius and angle corresponding to x and y Cartesian directions in the plane) and z (in the thickness direction). The in-plane perturbations in the outer layer of nodes were carried through in the column of nodes through the thickness of the sheet while the thickness perturbation applied only to the surface nodes away from the contact side. Only the thickness perturbation affected the tensile localization significantly; the 1% maximum perturbation was chosen to match the observation that a similar taper in tensile specimens was sufficient to ensure that most of the eventual tensile failures occur at the site of the reduction for these materials. Thus, the 1% taper was judged to be of approximately the same magnitude as internal flaws, machining irregularities, and so on. Type 3/shear localization failures showed little sensitivity to mesh perturbations, with a scatter of the front displacement to the maximum pulling load (U_m) and the front displacement to failure (U_f) less than 2 mm in all cases (the lower formabilities corresponding to the perturbed mesh).
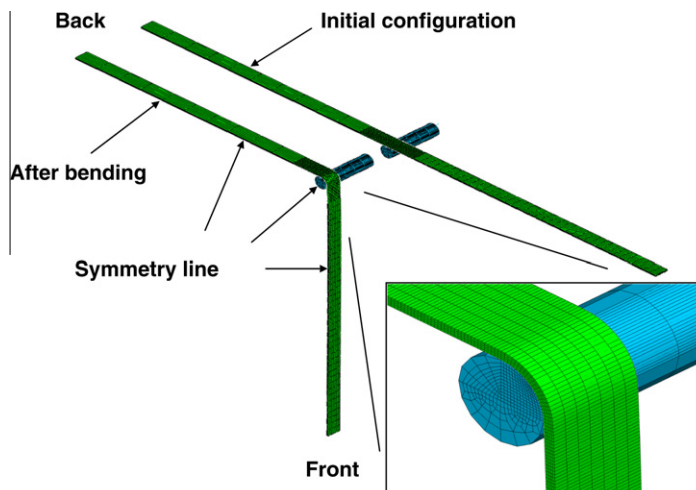

Fig. 4. Finite element mesh of the DBF test.

Simulations using a refined regular mesh were carried out to probe the adequacy of the mesh and consistency of the solution. The mesh shown in Fig. 4 was refined to obtain reduced element dimensions in the longitudinal, width, and thickness directions by half. The differences in the two simulations for a typical/severe case (DP780, R/t = 4.5, V_1 = 51 mm/s, V_2/V_1 = 0.3) were less than the experimental scatter: front engineering stress difference < 0.5 MPa (0.06%), front displacement to failure < 2 mm (4%). The penalty of this mesh refinement (by a factor of ∼8 in degrees of freedom) was a CPU time increase by a factor of 36 (1.2×10^4 s to 4.3×10^5 s).

The equilibrium and heat transfer equations are solved simultaneously using the H/V constitutive model to account for softening and altered strain hardening at elevated temperatures. Such capability was required because temperatures rise significantly above room temperature during draw-bend tests by deformation heating. The rate of heat input per unit volume, $\dot{q}$, is given by

$$\dot{q} = \eta\boldsymbol{\sigma} : \dot{\boldsymbol{\varepsilon}}, \tag{7}$$

where η is the fraction of plastic work converted to heat, with η = 0.9 measured for these alloys (Sung et al., 2010a), $\boldsymbol{\sigma}$ is the Cauchy stress tensor, and $\dot{\boldsymbol{\varepsilon}}$ is the plastic strain rate tensor.

The heat-transfer coefficient for metal-air contact was measured as 20 W/m² K by cooling a heated metal block in the air between 100 °C and room temperature and comparing the temperature drop with FE simulation. The heat-transfer coefficient for metal-metal contact is generally pressure dependent (Burte et al., 1990). But for simplicity, a constant value of 5 kW/m² K was used. The following thermal constants were determined using JMatPro (Sente-Software, 2007) based on chemical composition: thermal expansion coefficient: linear variation from 1.54×10^{-6} K⁻¹ at 25 °C to 1.58×10^{-6} K⁻¹ at 200 °C, heat capacity: linear variation from 0.45 J/g K at 25 °C to 0.52 J/g K at 200 °C, and thermal conductivity: piecewise linear variation of 36.7 W/m K at 25 °C, 36.9 W/m K at 70 °C, 36.8 W/m K at 100 °C and 36 W/m K at 200 °C. The accuracy of the thermal parameters was verified by performing tensile tests in air with attached thermocouples, and by performing draw-bend fracture and draw-bend springback tests while observing with an infrared camera (and a few cases with attached thermocouples). Corresponding simulations show agreement with measured temperatures, generally within 10 °C.
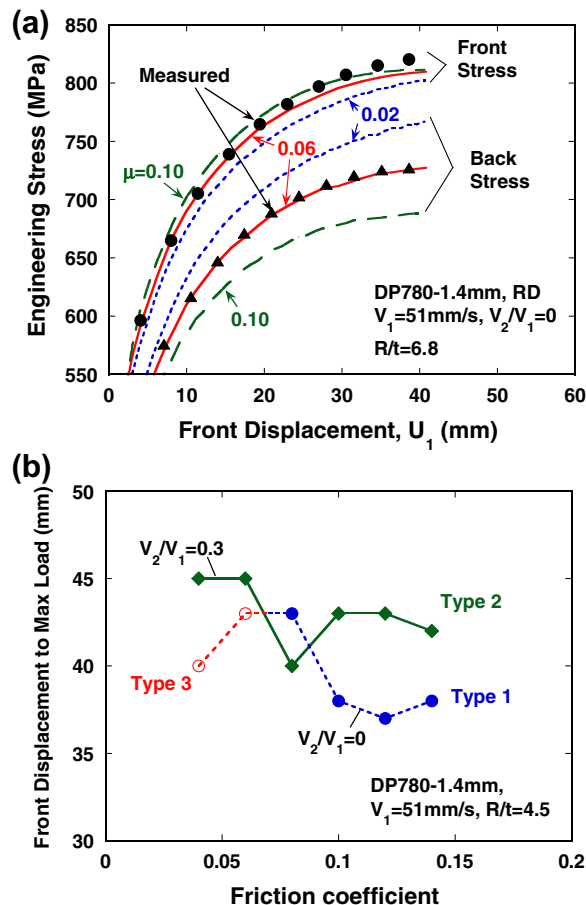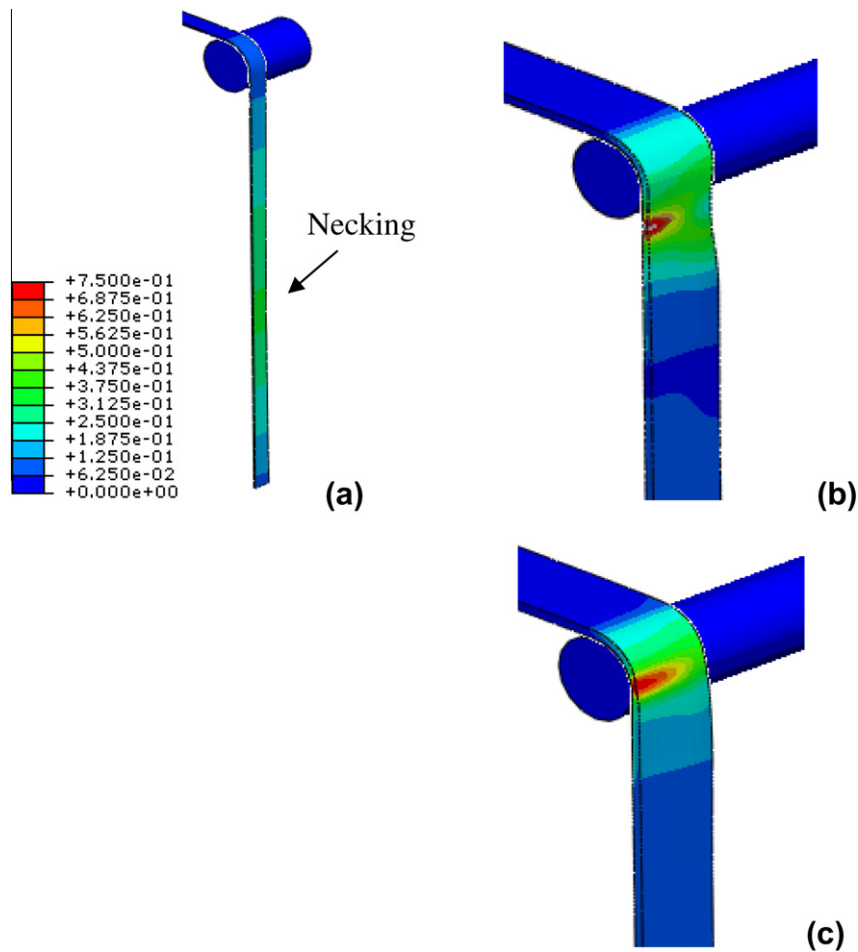

Fig. 5. Determination of best-fit friction coefficient from measured and simulated front and back forces (F_f, F_b).

Fig. 6. Predicted failure (color: equivalent plastic strain) of the thermo-mechanical solid model of: (a) Type 1, (b) Type 2, and (c) Type 3 failures.

The extreme thermal cases of the adiabatic condition (no heat transfer) and the isothermal condition (T = 25 °C, constant with time and position) were also considered. The adiabatic condition was enforced by setting insignificantly small values for heat-transfer coefficients, $h_{\text{adiabatic}}$ = 0.005 kW/m^2 K and $k_{\text{adiabatic}}$ = 0.037 W/m K (setting these values to 0.0 introduced non-convergence problems). The maximum temperature in blank in the model using $h_{\text{adiabatic}}$ = 0.005 kW/m^2 K was 3 °C higher than those using $h_{\text{adiabatic}}$ = 0.05 kW/m^2 K at the front displacement of 10 mm. This difference was judged insignificant for a factor-of-ten increase of heat-transfer coefficient, thus justifying use of the smaller value to approximate adiabatic conditions numerically. The isothermal condition was enforced by setting T = 25 °C in the constitutive model.

Coulomb friction coefficients (μ) were determined by comparing front and back engineering stresses throughout the test, as illustrated in Fig. 5(a) using a few values of μ. For this case, the best fit value of μ was 0.06, with an estimated uncertainty of 0.005 based on preferentially fitting to the back stress, which is more sensitive to friction changes. Fig. 5(b) shows that the friction coefficient significantly affects the simulated formabililily (front displacement to maximum load) and the type of simulated fracture. By carrying out procedures as illustrated in Fig. 5(a), the following friction coefficients were determined within an estimated experimental scatter of 0.005: μ = 0.12 (V_1 = 2.5 mm/s), μ = 0.1 (V_1 = 13 mm/s), μ = 0.065 (V_1 = 51 mm/s) except two DP980 cases: μ = 0.1 (R/t = 3.3), μ = 0.11 (R/t = 5.7).

The simulation begins by bending the sheet strip 90°, as shown in Fig. 4, mimicking the gripping procedure done by hand in the experiments. Then the drawing starts by moving the sheet ends at the specified velocities. The simulation proceeds until the front load decreased significantly by plastic localization/necking. The simulation was stopped when the load decreased from the maximum load by a fraction corresponding to the experimental observation. The fractional load drop ranged from 0% to 15%, depending on the material and the test conditions. This procedure determines the FE-predicted front grip displacement to failure, U_f. In this work, however, the front displacement to maximum load, U_m, is used to compare the results, rather than U_f. The reason for the use of U_m is that U_f is more sensitive than U_m to material scatter in the experiment, along with the element size and perturbation in the simulation. In addition, U_m and U_f are virtually the same for the shear fracture, Type 3, which represents the principal cases of interest.

5. Results

Fig. 6 show the three examples of the simulated failures. As explained in the introduction, the failure location was used to discern the failure type in the simulations (and is the primary determinant in the experiments). Fig. 6(a), (b) and (c) correspond to Type 1, Type 2, and Type 3, occurring at the unbent region, at the region below the tangent departure point, and within the region in contact with the roller, respectively. In all three cases, the predicted failure types match the experimentally observed ones.
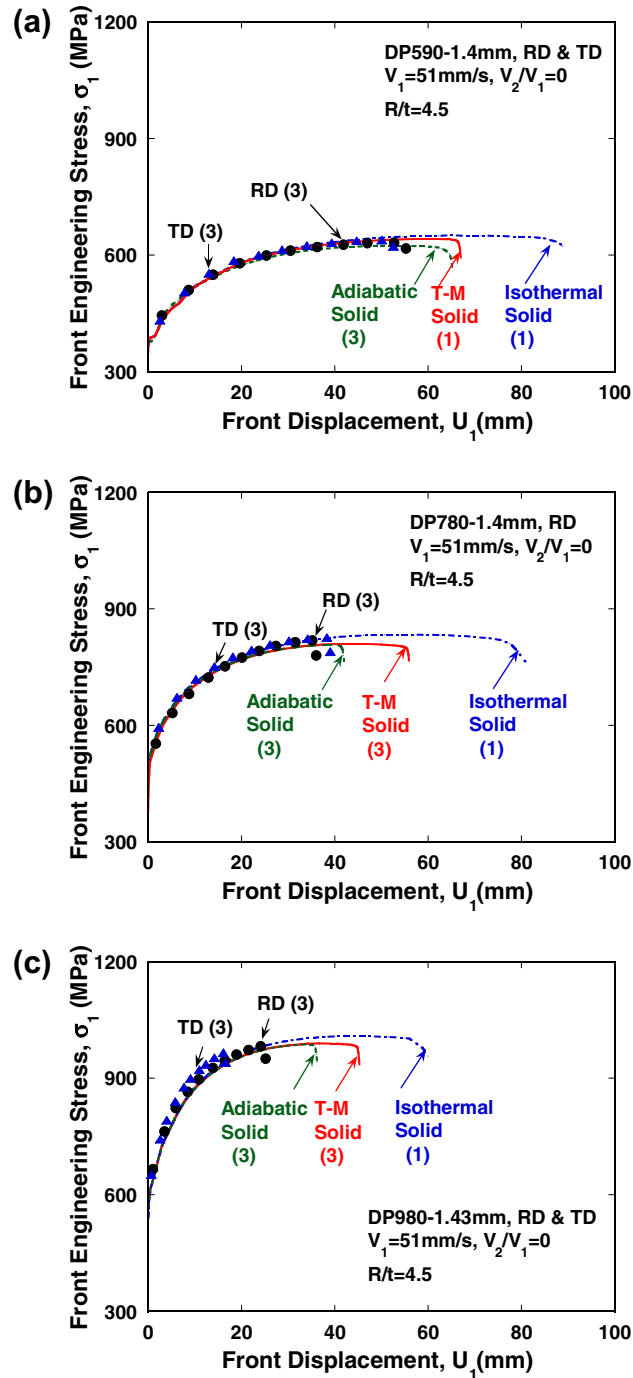

Fig. 7. Comparison of the experimental front stress vs. displacement with adiabatic, T–M, isothermal models: (a) DP590, V_1 = 51 mm/s, V_2/V_1 = 0; (b) DP780, V_1 = 51 mm/s, V_2/V_1 = 0; (c) DP980, V_1 = 51 mm/s, V_2/V_1 = 0.

Fig. 7 illustrate the detailed nature of the experimental results, the corresponding simulations, and the tabular results for formability that appear in Tables 4–7 using several alternative constitutive conditions. Because of space limitations, Tables 4 and 6 do not present results for all Type 1/tensile localization failures or Type 2/transitional failures, only one example of each is shown for the smallest R/t for which Type 1 or Type 2 failure was observed. The full list of tested R/t values is 2.2,

Table 4
Comparison of the observed and predicted failure elongation and failure type for $V_2/V_1 = 0$ draw-bend formability tests.

R/t	Experiments		Adiabatic			T–M			Isothermal			Modified T–M		
	U_m (RD)	U_m (TD)	U_m	Error		U_m	Error		U_m	Error		U_m	Error	
	(mm)	(mm)	(mm)	(mm)	(%)	(mm)	(mm)	(%)	(mm)	(mm)	(%)	(mm)	(mm)	(%)
DP 590, $V_1 = 51$ mm/s, $V_2/V_1 = 0$, $\mu = 0.065$														
2.2	30(3)	40(3)	34(3)	4	13	37(3)	7	23	47(3)	17	57	30(3)	0	0
3.3	38(3)	41(3)	49(3)	11	29	54(3)	16	42	64(3)	26	68	43(3)	5	13
4.5	52(3)	51(3)	60(3)	8	15	59(1)	7	14	65(1)	13	25	54(3)	2	4
5.7	55(1)		63(1)	8	15	60(1)	5	9	68(1)	13	24	58(1)	3	6
DP 780, $V_1 = 51$ mm/s, $V_2/V_1 = 0$, $\mu = 0.065$														
2.2	19(3)	15(3)	21(3)	2	11	22(3)	3	16	37(3)	18	95	20(3)	1	5
3.3	26(3)	29(3)	30(3)	4	15	34(3)	8	31	52(3)	26	100	30(3)	4	15
4.5	37(3)	40(3)	40(3)	3	8	43(3)	6	16	53(1)	16	43	39(3)	2	5
5.7	41(3)		44(1)	3	7	44(1)	3	7	54(1)	13	32	42(1)	1	2
6.8	41(1)		43(1)	2	5	41(1)	0	0	55(1)	14	34	43(1)	2	5
DP 980, $V_1 = 51$ mm/s, $V_2/V_1 = 0$, $\mu = 0.065$														
2.2	11(3)	2(3)	16(3)	5	46	18(3)	7	64	25(3)	14	127	15(3)	4	36
3.3	19(3)	12(3)	30(3)	11	58	35(3)	16	84	39(3)	20	105	29(3)	10	53
4.5	25(3)	17(3)	34(3)	9	36	37(3)	12	48	42(1)	17	68	33(3)	8	32
5.7	31(3)	24(3)	33(1)	2	7	32(1)	1	3	41(1)	10	32	32(1)	1	3

Notes: Values in the parentheses are predicted failure type.
Error percentages are based on RD DBF tests.

Table 5
Summary of predicted formability error for $V_2/V_1 = 0$ experiments, by failure type.

Materials	V_1 (mm/s)	Adiabatic (%)	T–M (%)	Isothermal (%)	Modified T–M (%)
Failure type 3					
DP590	51	19	26	50	6
DP590	13	12	30	46	10
DP590	2.5	−19	15	21	2
Average		4	24	39	6
DP780	51	10	18	67	7
DP780	13	15	42	97	34
DP780	2.5	0	74	109	57
Average		8	45	91	33
DP980	51	37	50	83	31
DP980	13	32	49	88	49
DP980	2.5	78	128	145	105
Average		48	75	105	62
Overall average		20	48	78	34
Failure type 1					
DP590	51	15	10	24	6
DP590	13	10	9	26	4
DP590	2.5	4	5	18	6
Average		10	8	23	5
DP780	51	5	−3	34	5
DP780	13	5	−6	23	3
DP780	2.5	−1	−3	26	−1
Average		3	−4	28	2
DP980	51	3	−2	18	0
DP980	13	13	7	32	16
DP980	2.5	11	5	32	14
Average		9	3	28	10
Overall average		7	2	26	6

Table 6
Comparison of the observed and predicted failure elongation and failure type for $V_2/V_1 = 0.3$.

R/t	Experiments		Adiabatic			T–M			Isothermal			Modified T–M		
	U_m (RD)	U_m (TD)	U_m	Error		U_m	Error		U_m	Error		U_m	Error	
	(mm)		(mm)	(mm)	(%)	(mm)	(mm)	(%)	(mm)	(mm)	(%)	(mm)	(mm)	(%)
DP 590, $V_1 = 51$ mm/s, $V_2/V_1 = 0.3$, $\mu = 0.065$														
2.2	36(3)		45(3)	9	26	45(3)	9	25	55(2)	19	53	35(3)	−1	−3
3.3	47(2)		59(2)	12	22	61(2)	14	30	75(2)	28	60	47(2)	0	0
4.5	55(2)		67(2)	12	22	68(2)	13	24	85(2)	30	55	61(2)	6	11
5.7	68(2)		45(3)	9	26	68(2)	0	0						
DP 780, $V_1 = 51$ mm/s, $V_2/V_1 = 0.3$, $\mu = 0.065$														
2.2	24(3)		25(3)	1	4	26(3)	2	8	46(2)	22	92	22(3)	−2	−8
3.3	31(3)		35(3)	4	13	36(3)	5	16	59(2)	28	90	31(3)	0	0
4.5	42(3)		43(2)	1	2	43(2)	1	2	69(2)	27	64	41(3)	−1	−2
5.7	51(2)		49(2)	−2	−4	50(2)	−1	−2	73(2)	22	43	47(2)	−4	−8
DP 980, $V_1 = 51$ mm/s, $V_2/V_1 = 0.3$, $\mu = 0.065$														
2.2	14(3)	6(3)	21(3)	7	50	25(3)	11	79	32(2)	18	129	18(3)	4	29
3.3	21(3)	11(3)	30(2)	9	43	35(2)	14	67	42(2)	21	100	26(3)	5	24
4.5	27(3)	14(3)	35(2)	8	30	46(2)	19	70	50(2)	23	85	33(2)	6	22
5.7	33(2)	18(2)	40(2)	7	21	50(2)	17	52	55(2)	22	67	39(2)	6	18

Table 7
Summary of predicted formability error for $V_2/V_1 = 0.3$ experiments, by failure type.

Materials	V_1 (mm/s)	Adiabatic (%)	T–M (%)	Isothermal (%)	Modified T–M (%)
Failure type 3					
P590	51	26	25	53	−3
DP590	13	13	18	46	−5
DP590	2.5	0	17	33	2
Average		13	20	44	−2
DP780	51	7	9	82	−4
DP780	13	5	6	87	10
DP780	2.5	−5	37	63	25
Average		2	17	77	11
DP980	51	41	72	105	25
DP980	13	42	54	108	30
DP980	2.5	103	131	216	141
Average		62	86	143	65
Overall average		26	41	88	25
Failure type 2					
DP590	51	22	14	57	6
DP590	13	5	5	34	−1
DP590	2.5	−4	10	24	0
Average		8	10	39	2
DP780	51	−4	0	43	−8
DP780	13	−9	−9	55	−2
DP780	2.5	−27	−3	25	4
Average		−14	−4	41	−2
DP980	51	21	21	67	18
DP980	13	12	21	67	17
DP980	2.5	0	16	53	28
Average		11	19	63	21
Overall average		2	8	48	7

3.3, 4.5, 5.7, 6.8, 7.9, 10.2, and 13.6. Tables 5 and 7, however, provide error statistics for all such Type 1 or Type 2 failures. Unless otherwise noted, all discussion applies to testing with the specimen aligned to the rolling direction (RD).

Fig. 7 and Tables 4 and 5 focus on the test condition $V_2/V_1 = 0$ which more nearly reproduces industrial practice than the $V_2/V_1 = 0.3$ condition. The $V_2/V_1 = 0$ condition also has the advantage of having more distinctive transitions of failure type from Type 1 ("tensile failure") to Type 3 ("shear failure"). The $V_2/V_1 = 0.3$ condition provides better experimental precision and reproducibility by having larger displacements to failure while encouraging a more reproducible frictional condition by
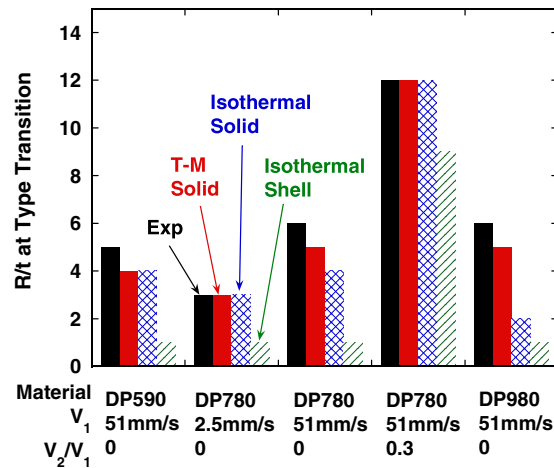
Fig. 8. Comparisons of R/t at failure type transition.

the large displacement of the strip relative to the tool at a nearly constant velocity. The principal difference between the two testing conditions is the large length of heated and strained material that has passed over the tool radius before failure occurs for the $V_2/V_1 = 0.3$ condition.

Several observations can be gleaned from the $V_2/V_1 = 0$ tests and simulations, Fig. 7 and Tables 4 and 5, as follows:

- The prediction of loads throughout the DBF test is excellent; the peak engineering stresses show a standard deviation between simulation and experiment of 14 MPa, while some deviation was observed between the predicted and measured U_f especially for Type 1. There is no suggestion of a systematic error of load-displacement curves in Fig. 6.
- There is a critical R/t ratio (R/t^*) for each material and pull rate (V_1) for the transition from Type 3 failure (shear) at small R/t to Type 1 failure (tension) for larger R/t. For R/t larger than this transition, the peak engineering stresses and displacements to failure are nearly constant (constant formability). For R/t smaller than the transition, the peak engineering stresses and displacements to failure are progressively reduced (reduced formability). Therefore, the transition value of R/t^* corresponds to a transition from constant peak pulling loads and displacements to progressively reduced ones.
- For Type 3 failures (shear), whether simulated or measured, the front displacement to failure (U_f) is essentially the same as the front displacement to the maximum pulling load (U_m). The differences are generally within 1 mm, or approximately the same as the test-to-test scatter. The largest differences observed were 3 mm. This is contrary to Type 1 (tensile) failures, which can exhibit significant displacements after the maximum front load occurs (with this observation in mind, the front displacement to maximum pulling load (U_m) will be used as the measure of formability for comparison of experiments and simulations.)
- Type 3 failures are promoted (and formability consequently decreased) by high pulling rates (and consequently high strain rates in bending). Comparison of DBF tests for DP 780 under identical conditions except for pulling rate, Table 4 illustrates a change of failure type and formability. Specifically, the transition occurs between R/t of 5.7 and 6.8 for $V_1 = 51$ mm/s, between R/t of 3.3 and 4.5 for $V_1 = 13$ mm/s, and between R/t of 2.2 and 3.3 for $V_1 = 2.5$ mm/s. The corresponding formabilities for R/t of 3.3 were 26, 38, and 38 mm, a reduction of formability of 32% as a result of higher pulling speed alone. Clearly, the thermal effects dominate the higher strain-rate sensitivity at higher strain rates, which tend to increase formability.
- Isothermal simulations (such as those used universally in industry) greatly over-predict the experimental formability for all Type 3 failures; much of the error is eliminated by thermo-mechanical or adiabatic simulation. On average, the failure elongations for Type 3 failures are over-predicted by 78%, 48%, and 20% by isothermal simulations, thermo-mechanical simulations, and adiabatic simulations, respectively (Table 5). This illustrates the dominant error introduced by relying on standard isothermal simulations: the error is reduced on average by a factor of 1.6–3.9 by including thermo-mechanical effects. Eliminating DP 980 from the averages (because of a postulated fracture mechanism for some R/t of DP 980 rather than plastic localization), the Type 3 failures are over-predicted by 65%, 34% and 6%, respectively, such that the error of predicted formability is reduced on average by a factor of 1.9–11 by including thermo-mechanical effects. Focusing only on the highest-rate tests for DP 590 and DP 780 (which still are only a fraction of $\sim$1/4–1/2 of typical industrial strain rates of 10/s) gives the following corresponding statistics: over-predictions of 59%, 22% and 14%, corresponding to reduced errors by factors of 2.9–2.
- The failure types and transitions among types (R/t^*) are generally predicted accurately using thermo-mechanical simulation, Fig. 8, but not using isothermal simulation or shell elements. Out of the 72 cases tested and simulated with $V_2/V_1 = 0$, 6 of the predicted types disagreed with the experimentally observed ones. All of these errors occurred just at the
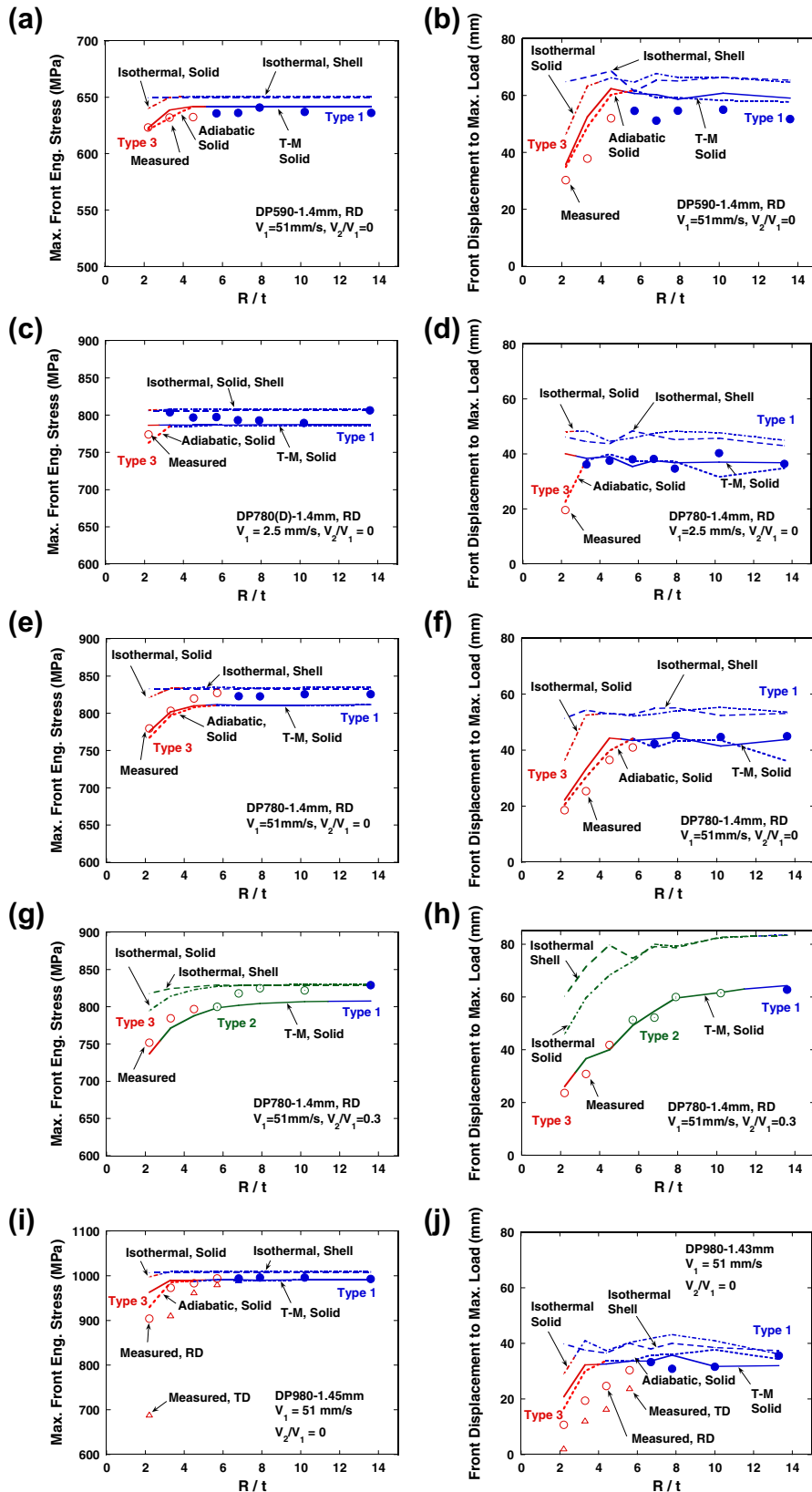
Fig. 9. Comparison of the front stresses (a, c, e, g, i) and displacements (b, d, f, h, j) at failure (a, b) DP590, V_1 = 51 mm/s, V_2/V_1 = 0; (c, d) DP780, V_1 = 2.5 mm/s, V_2/V_1 = 0; (e, f) DP780, V_1 = 51 mm/s, V_2/V_1 = 0; (g, h) DP780, V_1 = 51 mm/s, V_2/V_1 = 0.3; (i, j) DP980, V_1 = 51 mm/s, V_2/V_1 = 0.

Table 8
Summary of predicted formability errors.

Materials	Types	Number	Prediction error of U_m, %			
			Adiabatic	T–M	Isothermal	Modified T–M
All	All	144	14	25	60	18
All	Type 3	39	23	45	83	30
DP590, DP780	All	96	4	15	48	7
DP590, DP780	Type 3	23	7	27	63	12
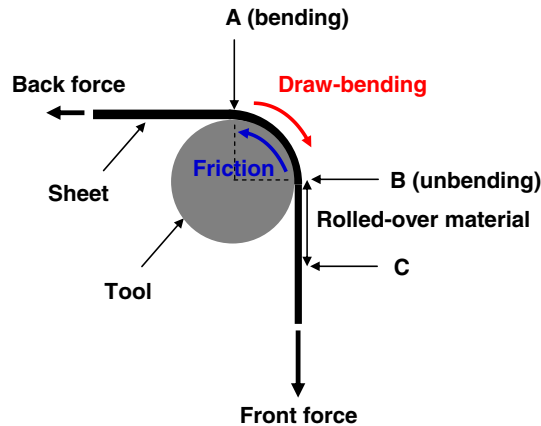
Fig. 10. Schematic of the draw-bend fracture test.

transitions of types between Type 1 and Type 3, and all of the simulations predicted Type 1 when Type 3 was observed. Put another way, for each of the few errors, the simulation predicted a Type 1 failure when a Type 3 failure occurred, but for the next smaller R/t available, the predictions and measurements were consistent (Type 3).

- For the two materials where testing was done in both rolling (RD) and transverse (TD) directions, DP 780 shows no significant difference while DP 980 shows much-reduced formability in TD. From testing of other alloys and directions, including three other examples of DP 980 steel, the DP 980 steel shown here is the only one that had a dramatic difference between RD and TD testing. The large change of formability with direction (with no corresponding change of constitutive equation) suggests that the DP 980 tested here undergoes brittle fracture (at sufficiently small R/t) related to its microstructure.

Fig. 9 summarize the experimental and simulation results of failure types, peak engineering stresses, and the front displacement to maximum load under conditions similar to Fig. 7. The left-hand figures plot the variation of simulated and measured peak engineering stresses with R/t while the corresponding right-hand figures report to front displacement to peak load (U_m) (recall that U_m is virtually indistinguishable from U_f for Type 3 failures, but not Type 1 failures).

The first impression is that the thermo-mechanical simulations capture all of the features of the experiments with impressive accuracy. Such agreement would be unlikely if the shear failures represented here were dominated by a mechanism (damage, brittle fracture) other than plastic localization. In particular, strain rate would be expected to have a minor role in brittle fracture.

The peak stresses and displacements U_m are clearly constant for R/t greater than R/t^*, and decrease progressively for values smaller than R/t^*. The R/t^* values are generally predicted by the thermo-mechanical simulations, within $\Delta R/t^*$ within variations of 0.5 or 1–2% of the peak engineering stresses.

Fig. 9 also emphasize the significant over-prediction of U_m from isothermal simulations, and the much better agreement with thermo-mechanical simulations. On average, the standard deviations of predicted and measured elongations to failure are 17 mm for isothermal simulations and 6 mm for thermo-mechanical simulations. However, the agreement is less impressive for DP 980 at small R/t, where presumably brittle failure related to the distribution of the large martensite constituent of this microstructure intervenes. Even for DP 980 at the smallest R/t, the magnitude of the differences between thermo-mechanical predictions and isothermal ones is comparable to the difference between thermo-mechanical prediction and measurements.

Turning briefly to the $V_2/V_1 = 0.3$ tests and simulations, these show for the first time Type 2 failures. These are quasi-tensile localizations that initiate and propagate in material that is weakened by thinning and increased temperature in a limited region of the strip that has undergone bending and unbending over the tool. As such, it is an artifact of the limited specimen width that is not often seen in industrial parts. Tables 6 and 7 show larger U_m, as expected, by approximately a factor of 1.33
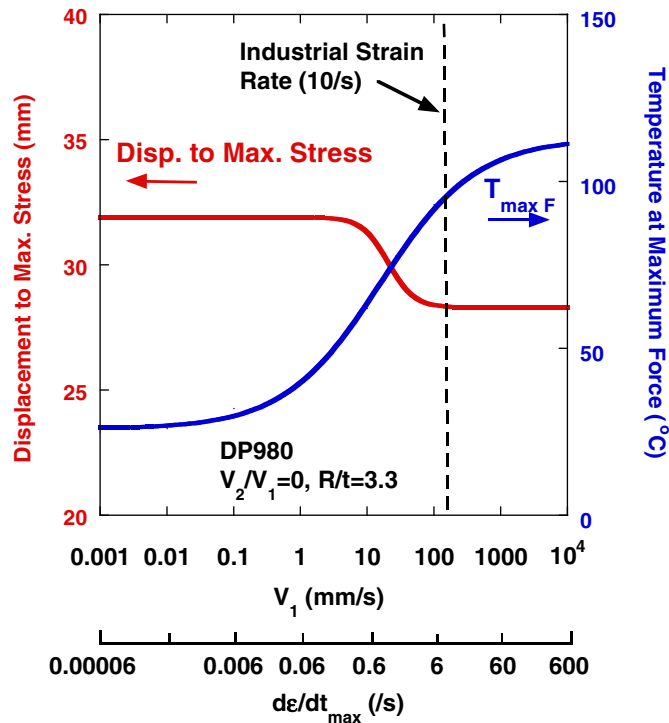
Fig. 11. The effect of front speed on the displacement to maximum load and temperature.

(1.38 for DP 590, 1.35 for DP 780), except for the fracture-prone DP 980, for which U_m increased by a factor of only 1.21. Type 2 and Type 3 failures are difficult to discern from simulations, so the fact that 8 out of 72 cases were mis-predicted is consistent with the 6 out of 72 mis-predicted for $V_2/V_1 = 0$ cases. Statistics of predicted formabilities from the various models are similar to the $V_2/V_1 = 0$ cases. The Type 3 failure displacements for DP 590 and DP 780 are over-predicted by 61%, 19% and 8%, respectively, by isothermal, thermo-mechanical, and adiabatic simulations, such that the error of predicted formability is reduced on average by a factor of 3.2–7.6 by including thermo-mechanical effects in the simulations.

6. Discussion

For the 144 experiments (RD only) and 576 finite element simulations represented by Tables 4–7, the overall error of the predictions formability (i.e. displacement to maximum load) are shown in Table 8. Taking the most pertinent data set for comparison, i.e. DP 590 and DP 780 tests exhibit Type 3/shear failure, the over-prediction of formability using isothermal simulation is 63%. This is reduced by more than half, to 27%, by the use of the thermo-mechanical simulations. Using the Modified H/V constitutive equation (which fits the tensile data equally well, but incorporates a larger change of stress at large strain and temperature that cannot be verified by currently-available testing methods), the 63% error is reduced to just 12%. This model also reduces error for Type 1 and Type 2 predictions, except for DP 980, for which brittle fracture is suspected.

Therefore, it may be concluded that the predominant phenomenon leading to over-predicted formability in industry of these AHSS is the ignoring of thermal effects in the simulations. A secondary consideration for some higher-strength alloys, such as the DP 980 tested here, is brittle fracture at small R/t, particularly in TD testing.

The three failure types – Type 1, 2, 3 – can be understood from a continuum mechanics viewpoint without introducing micro-structural features such as damage.

Fig. 10 shows a schematic of the draw-bend test. During draw-bending, material loaded in tension is bent near the entrance of the tooling (*A* in Fig. 10) and travels toward the exit of the tooling (*B* in Fig. 10) where unbending occurs. (Bending and unbending occur over a distance of approximately 3 times the sheet thickness, based on Eq. (1).) Because of friction and bending, the tensile force ramps up from the back force to the front force as the material moves around tool contact. The deformation state is near plane-strain because the materials in the back ligament hinder contraction in the width direction.

Type 3 failure occurs when the tension reaches the maximum value sustainable by the bent sheet, which is lower than the sustainable load in the straight pulling leg (i.e. the UTS), which is in tension. Type 3 failure is a result of localized necking during bending-under-tension (or possibly by a brittle stress/strain limit reached by the action of bending and increased tension around the contact region).
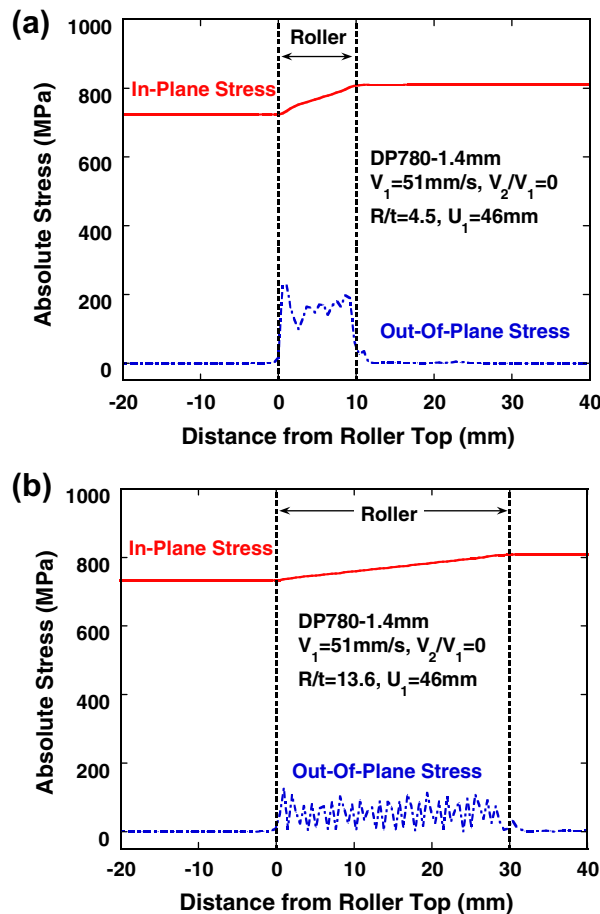
Fig. 12. The in-plane and out-of-plane stress distributions at a front displacement of 46 mm using the thermo-mechanical solid FE model for R/t of (a) 4.5, and (b) 13.6.

Type 1 failure occurs when the tension reaches the ultimate tensile strength of the material before the load limit is reached in the bending area. Type 1 failure is favored for large R/t and low drawing rates, both of which tend to raise the sustainable load in the bending region (where the peak local strains are higher, and thus temperatures are higher). Type 2 failure occurs in rolled-over materials (between B and C in Fig. 10). The stress state approaches uniaxial as the material moves away from the unbending region (B), but the material is softened by deformation-induced heating and thinning. Type 2 failure requires that a sufficient length of material is pulled over the tool such that the stress state is near uniaxial. This is favored by high ratios of V_2/V_1, which increase the pull-over distance for a given tensile load.

The role of pulling rate is to increase the peak strain rate in the material (Eq. (1)) and to reduce the time available for heat transfer. The strain rate effect inhibits strain localization while the thermal effect assists it (particularly in the bending/ unbending region where strains are high). Fig. 11 shows the FE-simulated effect of front velocity (and peak strain rate from Eq. (1) on the displacement to maximum load and the highest temperature at maximum load. The formability is nearly constant for V_1 up to 1 mm/s. Between 1 and 100 mm/s, the formability drops precipitately from 32 to 28 mm as the adiabatic limit is approached, while the highest temperature at maximum load shows a steady increase. The dashed vertical line in Fig. 11 represents the bending strain rate in a typical industrial sheet operation, 10/s, which is above that required to get the full adiabatic effect.

It is notable that the shell elements predicted shear failure poorly, as shown in Figs. 8 and 9. The inability of FE forming simulations using shell elements can be understood by reference to Figs. 12 and 13. Fig. 12 shows how the out-of-plane (through-thickness) stress varies as material elements traverse contact with the tool. The value is much greater for small R/t, as expected, while for shell elements this stress is always identically zero. Thus, for small R/t where shear fracture is important, shell elements do not capture the proper stress distribution. Fig. 13 illustrates the problem further by comparing the thickness variation as material is pulled over the tool, as simulated by solid and shell elements. While there is little difference for isothermal and thermo-mechanical solid elements, the isothermal shell shows much less thickness variation and thus greatly over-predicts formability for small R/t cases.
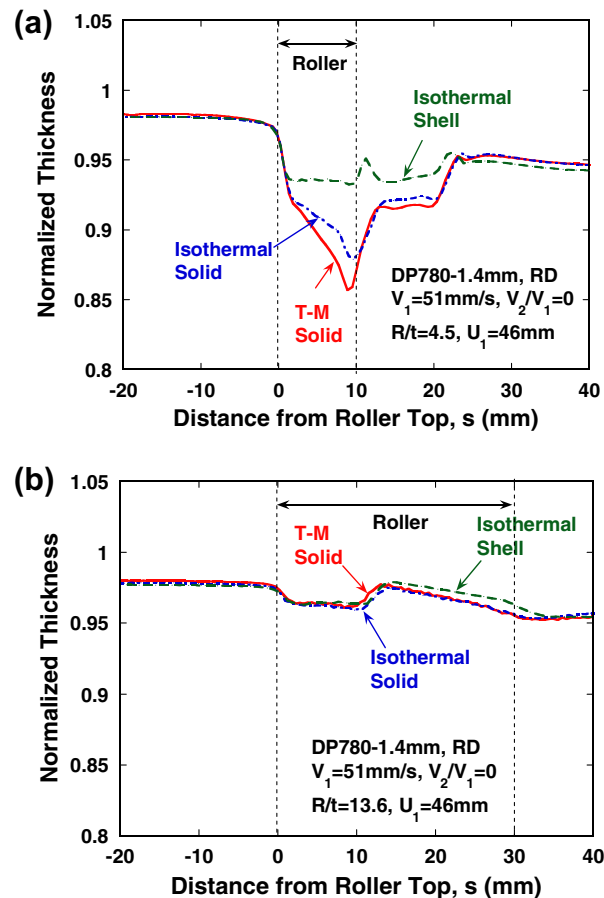
Fig. 13. The calculated thickness distributions at a front displacement of 46 mm for R/t of: (a) 4.5 and (b) 13.6.

7. Summary and conclusions

More than 144 draw-bend formability tests of three dual-phase steels (DP 590, DP 780 and DP) and more than 576 finite element simulations were conducted. The finite element simulations made use of 3-D solid element and thermo-mechanical coupling under various thermal conditions, with some comparisons using shell elements (similar to industrial practice). The purpose was to understand the origin of so-called "shear fracture" and the inability to predict its appearance in sheet forming operations using standard industrial techniques. The following conclusions were reached:

- The principal error in predicting shear fracture using current industrial technology lies in ignoring the role of deformation-induced heating. The high temperatures (typically 100 °C) attained near (but not at) the final fracture are what distinguish advanced high strength steels (AHSS), with their remarkable combinations of high strength and high ductility, from past sheet forming alloys. In a general sense, deformation-induced heating can be thought of as "causing" shear fractures in AHSS. The magnitudes of the errors attributable to ignoring deformation-induced heating are illustrated by comparing the percentage that shear fracture is over-predicted for DP 590 and DP 780 steels by isothermal simulations (63%) vs. thermo-mechanical simulations based on tensile tests only (27%) vs. thermo-mechanical simulations using an modified constitutive model (12%). That is, simply including thermo-mechanical effects in FE predictions of failure reduces the error of prediction by a factor of 2–5. Furthermore, the type of failure was predicted accurately for 90% of the tests, with the ones in error just at the boundary between failure types.
- Accurate knowledge of the material constitutive equation in terms of strain, strain-rate, and temperature is essential for predicting forming performance. The recently-introduced "H/V Model" (Sung et al. 2010a) worked well in the simulations performed here.
- Industrial conditions are expected to further accentuate strain rate effects. The typical peak strain rate in bending for an industrial forming operation, 10/s, is several times higher that those achieved in the testing performed here. Industrial forming under such conditions is very close to adiabatic. It is possible to improve formability greatly by lowering strain rates, thus promoting isothermality, but such approaches may be impractical.

- Thermo-mechanical modeling with solid elements was able to predict all the significant trends in draw-bend formability in terms of bending ratio (R/t), although quantitative predictions were considerably worse for DP 980, the strongest steel tested (the modeling also reproduced measured temperature rises to within 10 °C).
- The ability to predict shear fracture with thermo-mechanical FEM does not normally require invocation of arbitrary damage mechanisms or brittle fracture, which are normally second-order effects for sheet metal forming failures that occur after localization is well developed. However, for the DP 980 tested here, damage and fracture approaches may be essentially to reproduce the behavior.
- The DP 980 tested here is a special case. It exhibited very anisotropic fracture properties with virtually no plastic anisotropy. Testing in the TD caused much earlier shear fracture that in the RD, but both could be earlier than predicted by FE modeling. Three other DP 980 alloys tested (and the DP 590 and DP 780 alloys presented here) separately did not show this behavior. It was concluded that the DP 980 tested here exhibits a kind of micro-structural "brittle fracture," particularly when testing in the TD.
- The results suggest that three distinct fracture criteria will need to be applied in industry to predict the range of failures that can occur with AHSS:
    o Large R/t fracture (e.g. forming limit diagram, tensile-type strain localization).
    o Small-R/t fracture/shear fracture (as simulated and tested here, bending-under-tension-type strain localization).
    o Damage/brittle fracture, before strain localization (various microstructurally-based models, like for DP 980 tested here).
- The foregoing conclusions suggest that effective prediction of failures of AHSS under industrial forming.
- Shear fractures (i.e. those occurring in low R/t regions preferentially) occur almost immediately (within 1 mm of displacement) after the maximum load is achieved, i.e. there is essentially no post-uniform elongation. This is contrary to the tensile behavior of the same alloys. This implies that the maximum load point can be used as an accurate gage of total formability for shear fracture, as postulated earlier in the literature (Yoshida et al., 2005; Hudgins et al., 2010).
- Friction plays an important role in determining the type of failure and the formability.
- Shear fractures are predictable with continuum-based FE simulations. The principal remaining problem for industrial application is the poor performance of shell elements (almost universally used in industry) for small-R/t fracture. The importance of through-thickness stresses and thickness changes were illustrated using solid and shell simulations.
- Improved accuracy in predicting shear failure will require improved constitutive information, particularly at large strain (up to 0.5) and elevated temperature (up to 100 °C) for alloys under considerations. There are apparently no elevated-temperature balanced-biaxial tests currently available suitable for the measurement of stress–strain of AHSS for normal thickness.

Acknowledgements

Appendix A

The maximum true strain occurring in the draw-bend fracture test, ε_{max}, is the bending strain on the outer fiber of the sheet during bending. If the neutral plane is assumed to be located on the inner surface of the sheet, that is if the sheet tension is sufficient to yield the sheet on the inner fiber, then ε_{max} is given by

$$\varepsilon_{max} = \ln(1 + t/R), \tag{A1}$$

where t is the initial sheet thickness and R is the roller radius. The travel displacement to attain this strain was obtained from the FE simulations of the DBF test under a wide range of conditions (Wagoner et al., 2009b):

$$d_{bend} \approx 3t. \tag{A2}$$

If the material element on the outer fiber during bending is assumed to travel at the same speed as the front grip, V_1, the maximum strain rate can be expressed as:

$$\dot{\varepsilon}_{max} = \frac{\varepsilon_{max} V_1}{3t} = \frac{V_1}{3t} \ln(1 + t/R). \tag{A3}$$

References

Bai, Y., Wierzbicki, T., 2008. Predicting fracture of AHSS sheets on the punch and die radii and sidewall. In: Numisheet 2008, September 1–5, 2008, Interlaken, Sweden, pp. 297-306.

Bhattacharya, B., 2006. An overview of advanced high strength steels (AHSS), In: Wagoner, R.H., (Ed.), Report: Advanced High Strength Steel Workshop, October 31, 2006, pp. 38–59. <http://mse.osu.edu/~wagoner/AHSS/AHSSReportFINAL.pdf>.

Burte, P.R., Im, Y.T., Altan, T., Semiatin, S.L., 1990. Measurements and analysis of the heat transfer and friction during hot forging. J. Eng. Ind. 112, 332–339.

Carden, W.D., Geng, L.M., Matlock, D.K., Wagoner, R.H., 2002. Measurement of springback. Int. J. Mech. Sci. 44, 79–101.

Chen, X.M., DU, C., Wu, X., Zhu, X., Liu, S.-D., 2009, Sheet metal shearing and edge characterization of dual phase steels. In: International Deep Drawing Research Group 2009, Golden, USA, pp. 809–823.

Chen, X., Shih, H.C., Luo, M., Shi, M.F., Wierzbicki, T., 2010. AHSS shear fracture predictions based on a recently developed fracture criterion, SAE International, Paper 2010-01-0988.

Choi, K.S., Liu, W.N., Sun, X., Khaleel, M.A., Fekete, J.R., 2009. Influence of manufacturing processes and microstructures on the performance and manufacturability of advanced high strength steels. Trans. ASME: J. Eng. Mater. Technol. 131, 041205-1–041205-9.

Damborg, F.F., Wagoner, R.H., Danckert, J., Matlock, D.K., 1997. Stretch-bend formability. In: Proceedings of the MP2M-Center Seminar, Danish Technical University, pp. 9.1–9.7, Publication No. MM97.81.

Damborg, F.F., Nielsen, K.B., Danckert, J., Wagoner, R.H., 1998. Application of ductile fracture criteria to bending under tension, Sheet Metal Forming Beyond 2000 (20th IDDRG), Centre de Recherches Métallurgiques, pp. 145–155.

Fekete, J., 2009. Private communication, 30001 Van Dyke Ave., Warren, MI, USA.

Ghosh, A.K., 1975. The effect of lateral draw-in on stretch formability. Met. Eng. Q., 53–64.

Hecker, S.S., 1974. A reproducible cup test for assessing sheet metal stretchability. Met. Eng. Q., 30–36.

Heimbuch, R., 2006. An overview of the auto/steel partnership researcch needs. In: Wagoner, R.H., (Ed.), Report: Advanced High Steel Strength Workshop, October 31, 2006, pp. 14–23. <http://mse.osu.edu/~wagoner/AHSS/AHSSReportFINAL.pdf>.

Hora, P., Tong, L., 2008. Theoretical prediction of the influence of curvature and thickness on the FLC by the enhanced modified maximum force criterion. In: Numisheet 2008, September 1–5, 2008, Interlaken, Switzerland.

Hudgins, A.W., Matlock, D.K., Speer, J.G., Van Tyne, C.J., 2010. Predicting instability at die radii in advanced high strength steels. J. Mater. Process. Technol. 210, 741–750.

Kadkhodapour, J., Butz, A., Ziaei-Rad, S., Schmauder, S., 2011. A micro mechanical study on failure initiation of dual phase steels under tension using single crystal plasticity model. Int. J. Plasticity. doi:10.1016/j.ijplas.2010.12.001.

Keeler, S.P., Backofen, W.A., 1963. Trans. ASM 56, 25–58.

Kim, C.H., Bandar, A.R., Yang, Y.P., Sung, J.H., Wagoner, R.H., 2009. Failure analysis of advanced high strength steels (AHSS) during draw bending. In: Levy, B.S., Matlock, D.K., Van Tyne, C.J., (Eds.), Proceedings of the IDDRG: Mat. Prop. Data for More Effective Num. Anal., Colorado School Mines, pp. 449–460. ISDN: 978-0-615-29641-8.

Krauer, J., Hora, P., 2009. Thermoactive process modeling of deep drawing with austenitic strainless steel. In: IDDRG 2009 International Conference, June 1–3, 2009, Golden, CO, USA.

Krempaszky, C., Ocenasek, J., Espinoza, V., Werner, E., Hebesberger, T., Pichler, A., 2007. Micromechanical modeling of the formability of dual-phase steels, MS&T Conference, Detroit, MI, USA, p. 31-43.

Li, K., Geng, L., Wagoner, R.H., 1999. Simulation of springbank: choice of elements. In: Geiger, M. (Ed.), Advanced Technology of Plasticity, vol. III. Springer, Berlin. pp. 2091–2098.

Li, K.P., Carden, W.P., Wagoner, R.H., 2002. Simulation of springback. Int. J. Mech. Sci. 44, 103–122.

Li, Y., Luo, M., Gerlach, J., Wierzbicki, T., 2010. Prediction of shear-induced fracture in sheet metal forming. J. Mater. Process. Technol. 210, 1858–1869.

Ma, N., Park, T., Kim, D., Kim, C., Chung, K., 2010. Numerical and experimental evaluation of the impact performance of advanced high-strength steel sheets based on a damage model. Met. Mater. Int. 16, 427–439.

Matlock, D.K., 2006. Microstructural aspects of advanced high strength steels. In: Wagoner, R.H., (Ed.), Report: Advanced High Strength Steel Workshop, October 31, 2006, pp. 60–72. <http://mse.osu.edu/~wagoner/AHSS/AHSSReportFINAL.pdf>.

Nakajima, K., Kikuuma, T., Hasuka, K., 1971. Yawata Technical Report No. 284, Yawata, Japan, pp. 678–690.

Sente-Software, 2007. JMatPro: Practical Software for Materials Properties, Surney Tech. Center, UK.

Sklad, M.P., 2008. Analysis of deformation in the shear and shear-tension tests. In: Numisheet 2008, Interaken, Switzerland, pp. 91–95.

Sriram, S., Urban, D., 2003. Formability characterization of a new generation of high strength steels. In: AISI/DOE Technology Roadmap Program, US Department of Energy, Oak Ridge, TN, USA.

Stoughton, T., Xia, C., Du, C., Shi, M.F., 2006. Challenges for constitutive models for forming of advanced steels. In: Wagoner, R.H., (Ed.), Report: Advanced High Strength Steel Workshop, October 31, 2006, pp. 73–80. <http://mse.osu.edu/~wagoner/AHSS/AHSSReportFINAL.pdf>.

Sung, J.H., Kim, J.H., Wagoner, R.H., 2010a. A plastic constitutive equation incorporating strain strain-rate, and temperature. Int. J. Plasticity 26, 1746–1771.

Sung, J.H., Kim, J.H., Wagoner, R.H., in preparation. The formability of advanced high strength steels using draw-bend formability tests (unpublished research).

Vallance, D.W., Matlock, D.K., 1992. Application of the bending-under-tension friction test to coated sheet steels. J. Mater. Eng. Perform. 1, 685–693.

Wagoner, R.H., 2006. Advanced high-strength steels: fundamental research issues. In: Wagoner, R.H., (Ed.), Proceeding of NSF Workshop, October 22–23, 2006, Arlington, VA.

Wagoner, R.H., Chan, K.S., Keeler, S.P., (Eds.), 1989. Forming Limit Diagrams: Concepts, Methods, and Applications, The Metallurgical Society, pp. 167–182.

Wagoner, R.H., Carden, W.D., Carden, W.P., Matlock, D.K., 1997 (Springback after drawing and bending of metal sheets). In: Chandra, T., Leclair, S.R., Meech, J.A., Verma, B., Smith, M., Balachandran, B. (Eds.), Proceedings of the IPMM'97-Intelligent Processing and Manufacturing of Materials, vol. 1. University of Wollongong, pp. 1–10.

Wagoner, R.H., Madeshia, A., Sung, J.H., Kim, J.H., 2009a. Plasticity and failure of advanced high strength steels. In: Macro- to Nano-scale Inelastic Behavior of Materials: Plasticity, Fatigue, and Fracture, (Procs. Plasticity 2009), Neat Press, pp. 145-147. ISBN:0-9659463-9-8.

Wagoner, R.H., Kim, J.H., Sung, J.H., 2009b. Formability of advanced high strength steels. In: Proceedings of the Esaform 2009, U. Twente, Netherlands, CD.

Walp, M.S., Wurm, A., III, J.F.S., and Desai, A.K., 2006, Shear fracture in Advanced High Strength Steels, SAE Technical Publication, Warrendale, PA.

Wenzloff, G.J., Hylton, T.A., Matlock, D.K., 1992. A new procedure for the bending under tension friction test. J. Mater. Eng. Perform. 1, 609–613.

Wu, J., Zhou, D.J., Zhang, L., Zhou, Y.J., Du, C.Q., Shi, M.F., 2006. A failure criterion for stretch bendability of advanced high strength steels, SAE International, Paper 2006-01-0349.

Xia, Z.C., Stoughton, T.B., Du, C., Shi, M.F., 2006. Challenges in failure prediction in forming advanced high-strength steels. In: Wagoner, R.H., (Ed.), Report: Advanced High Strength Steel Workshop, October 31, 2006, pp. 81–87. <http://mse.osu.edu/~wagoner/AHSS/AHSSReportFINAL.pdf>.

Yoshida, M., Yoshida, F., Konishi, H., Fukumoto, K., 2005. Fracture limits of sheet metals under stretch bending. Int. J. Mech. Sci. 47, 1885–1896.